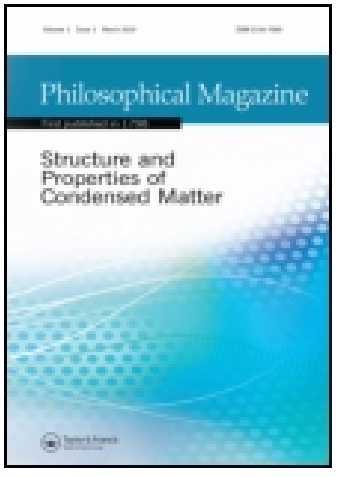

Philosophical Magazine
Publication details, including instructions for authors and subscription information:
http://www.tandfonline.com/loi/tphm20

Atomic-resolution spectroscopic imaging of oxide interfaces

L. Fitting Kourkoutis [a], H.L. Xin [b], T. Higuchi [c], Y. Hotta [c d], J.H. Lee [e f], Y. Hikita [c], D.G. Schlom [e], H.Y. Hwang [c g] & D.A. Muller [a h]

[a] School of Applied and Engineering Physics, Cornell University, Ithaca, USA
[b] Department of Physics, Cornell University, Ithaca, USA
[c] Department of Advanced Materials Science, University of Tokyo, Kashiwa, Japan
[d] Correlated Electron Research Group, RIKEN, Saitama, Japan
[e] Department of Materials Science and Engineering, Cornell University, Ithaca, USA
[f] Department of Materials Science and Engineering, Pennsylvania State University, University Park, USA
[g] Japan Science and Technology Agency, Kawaguchi, Japan
[h] Kavli Institute at Cornell for Nanoscale Science, Ithaca, USA
Published online: 20 Oct 2010.

To cite this article: L. Fitting Kourkoutis, H.L. Xin, T. Higuchi, Y. Hotta, J.H. Lee, Y. Hikita, D.G. Schlom, H.Y. Hwang & D.A. Muller (2010) Atomic-resolution spectroscopic imaging of oxide interfaces, Philosophical Magazine, 90:35-36, 4731-4749, DOI: 10.1080/14786435.2010.518983

To link to this article: http://dx.doi.org/10.1080/14786435.2010.518983

Philosophical Magazine
Vol. 90, Nos. 35–36, 14–28 December 2010, 4731–4749

Atomic-resolution spectroscopic imaging of oxide interfaces

L. Fitting Kourkoutis[a]*, H.L. Xin[b], T. Higuchi[c], Y. Hotta[cd], J.H. Lee[ef], Y. Hikita[c], D.G. Schlom[e], H.Y. Hwang[cg] and D.A. Muller[ah]

[a]*School of Applied and Engineering Physics, Cornell University, Ithaca, USA;* [b]*Department of Physics, Cornell University, Ithaca, USA;* [c]*Department of Advanced Materials Science, University of Tokyo, Kashiwa, Japan;* [d]*Correlated Electron Research Group, RIKEN, Saitama, Japan;* [e]*Department of Materials Science and Engineering, Cornell University, Ithaca, USA;* [f]*Department of Materials Science and Engineering, Pennsylvania State University, University Park, USA;* [g]*Japan Science and Technology Agency, Kawaguchi, Japan;* [h]*Kavli Institute at Cornell for Nanoscale Science, Ithaca, USA*

(*Received 2 November 2009; final version received 24 August 2010*)

Perovskite oxides show a rich variety of electronic phases in bulk. The prospect of combining these phases at the atomic scale has fueled the interest in oxide heterostructures. The existence of interfaces can, however, greatly affect the macroscopic properties of these structures, leading on the one hand to exotic new phases stabilized at the interface or on the other hand to the degradation of bulk-like properties. With recent advances in electron microscopy the composition and bonding at such buried interfaces can now be imaged with atomic resolution. The bonding information is obtained from the near-edge fine-structure of core-level electron energy loss spectra. Here, we discuss the near-edge fine-structure focusing on the O-*K* and transition metal $L_{2,3}$ edges which are of particular importance for the family of perovskite oxides. Spectroscopic imaging of a vanadate/titanate heterostructure demonstrates the capability of the technique to characterize atomic-scale interdiffusion at interfaces. Resolution limits in spectroscopic imaging due to inelastic delocalization effects are discussed.

Keywords: scanning transmission electron microscopy; electron energy loss spectroscopy; spectroscopic imaging; perovskites; interface properties

1. Introduction

The structurally-related family of perovskite oxides exhibits an almost universal range of electronic properties. Insulating, semiconducting, metallic, superconducting, ferromagnetic, antiferromagnetic, ferroelectric, and piezoelectric oxides exist, many of which are lattice-matched within a few percent of each other, giving rise to the possibility of heteroepitaxial structures accessing these multiple degrees of freedom [1–3]. When joining two complex oxides at the atomic scale, exotic phases can be stabilized at the interface which can greatly affect the macroscopic properties of the material and presents a unique opportunity to create new artificial states

*Corresponding author. Email: lf56@cornell.edu

ISSN 1478–6435 print/ISSN 1478–6443 online

DOI: 10.1080/14786435.2010.518983
http://www.informaworld.com

between two materials [4–9]. Recent examples include interface ferromagnetism induced between two paramagnets [10] and conducting and even superconducting interfaces induced between two insulators [4,5,8]. Techniques that study structural, chemical and bonding changes across interfaces such as the combination of scanning transmission electron microscopy (STEM) and electron energy loss spectroscopy (EELS) are invaluable for the understanding of phenomena that occur at these complex-oxide interfaces.

In STEM, a small (0.1–0.2 nm) electron beam is focused and then scanned across an electron-transparent sample [11,12]. As the electron propagates through the sample it can interact with the material and undergo elastic and inelastic scattering. In high-angle annular-dark-field (HAADF) imaging, electrons that are scattered to high angles are detected on an annular detector [13,14]. For thin samples, the image intensity approximately scales with the scattering cross-section as $Z^{1.7}$, where Z is the atomic number [15]. Due to this strong dependence of the image intensity on the atomic number, the HAADF imaging mode is often referred to as Z-contrast imaging. For thicker crystalline samples, however, channeling along atomic columns can greatly affect the image contrast [13,16,17] and lead to an increased visibility of an adatom [16] or dopant atoms [18]. Similarly, atomic disorder or lattice distortions can result in a reduction of the contrast by dechanneling off the atomic column [19–21], an effect that has been exploited to image individual oxygen vacancies in a zone-axis oriented crystal [22]. The interpretation of HAADF images as Z-contrast images is therefore only a first approximation, where effects such as channeling and lattice distortions are not taken into account. For quantitative measurements, image simulations are often needed which take into account the sample thickness, crystal orientation, lattice distortions, detector geometry and the evolution of the electron probe in the sample.

One of the advantages of using an annular detector is that the center hole allows electrons which are scattered to low angles to pass through making possible simultaneous HAADF imaging and electron energy loss spectroscopy (EELS), in which the inelastically scattered electrons are analyzed according to their energy loss [23–28].

For typical sample thicknesses of 10–20 nm, the spatial resolution of HAADF images is dominated by the size of the electron probe which is set by the aberrations of the probe forming lens, the electron wavelength and the effective source size. Today, atomic-resolution is routinely obtained, and with the correction of electron–optical aberrations, sub-angstrom imaging is now possible [29,30]. Resolution improvement is, however, not the only benefit of aberration correction. By correcting the electron–optical aberrations up to third- or even fifth-order the probe-forming aperture can be opened up and for the same probe size the beam current can be greatly enhanced. With the increase in beam current and a large enough collection angle, a single core-loss EELS spectrum, with a signal-to-noise ratio that allows the extraction of bonding information, can be recorded in milliseconds; a full two dimensional (2D) map in under a minute [31].

Atomic-resolution spectroscopic imaging greatly benefits from this increase in acquisition speed, as typical sample drift rates of $\sim$5 Å/min can pose serious problems if 1–10 seconds are required to record a single spectrum with sufficient signal to noise ratio. Despite this, small atomic-resolution composition maps have

been demonstrated on uncorrected systems [24,32]; however, these maps can take hours to record and significant drift correction is necessary.

A probe corrector allows for larger beam currents in smaller probes; however, at the same time the collection efficiency of the EELS spectrometer needs to be optimized so that the additional current can enter the spectrometer. More than a loss in current, small collection angles can also introduce artifacts because the incoherent imaging approximation no longer holds [33–35]. Diffraction contrast and elastic scattering artifacts can appear and even dominate the spectroscopic image [36–38]. Strong elastic scattering on heavy-atom columns can prevent inelastically scattered electrons from entering the spectrometer and result in contrast reversals and inelastic images that are dominated by the elastic scattering. Opening up the collection angle, so that most of the elastically scattered electrons enter the spectrometer, will suppress these effects. At such large angles, the energy resolution can, however, degrade and additional corrective optics might be necessary to preserve the energy resolution at large collection angles [31,39].

Advances in electron optics have therefore allowed spatially resolved EELS to enter the era of 2D imaging of composition and bonding at the atomic-scale. Microscopic inhomogeneities and atomic-scale interdiffusion can now readily be characterized. Atomic-resolution spectroscopic imaging is, however, limited to material systems which can withstand the high electron beam doses needed, i.e. no radiation damage during the data acquisition. Extra effort is devoted to imaging and EELS mapping using lower accelerating voltages (60 keV or less) to minimize knock-on damage [40].

Before demonstrating the capabilities of spectroscopic imaging of oxide heterointerfaces, we will set the stage by discussing core-level EELS of perovskite oxides and the resolution limits for core-level spectroscopic imaging.

2. Core-level electron energy loss spectroscopy of perovskite oxides

Core-level ionization edges in an EELS spectrum occur within a range of ~50 eV to several thousand eV and involve the excitation of electrons from a core orbital to unoccupied states above the Fermi level. Since the core electron binding energies are specific for each element and type of subshell, it is possible to obtain information about the elemental composition of a sample. Furthermore, the fine-structure of an ionization edge can give information on bonding, coordination and interatomic distances.

In the simplest model for core-level transitions, only single-particle transitions from a localized core state to a final unoccupied state are considered. In addition, one typically assumes small momentum transfer, i.e. the scattering is restricted to very small angles for which the dipole approximation is valid. In this picture, the energy-loss near-edge structure (ELNES) of a core-level EELS edge can be interpreted as the local density of empty states above the Fermi level, partitioned by angular momentum (due to the dipole selection rules which limit the transitions from a core state with orbital angular momentum l to final states with angular momentum $(l \pm 1)$), by element (since the energy is measured with respect to the unique binding energy of the core state) and by site (if the EELS measurement is

performed with a localized probe in a STEM) [41–43]. However, many-body effects, in particular the effect of the core-hole that is created during the excitation process, plural scattering and broadening of the local density of states (LDOS) due to the finite lifetime of the core-hole and the excited final state, have to be taken into account to understand the features of a core-level edge.

The core-hole effect is in particular important for the transition metal $L_{2,3}$ edges, because of strong coupling between the $2p$ core-hole and the $3d$ electrons. For the O-K edge, on the other hand, the $1s$ core hole has smaller effects on the spectral shape as will be discussed below.

2.1. $L_{2,3}$ *edges in 3*d *transition metal oxides*

For $L_{2,3}$ edges transitions from an initial $2p$ state to final states of both s- and d-character are allowed according to the dipole selection rule. The radial overlap of the initial $2p$ and the $3d$ states is, however, significantly larger than the overlap of the $2p$ and $4s$ states. Additionally, the density of states (DOS) of the $4s$ band is considerably lower than that of the $3d$ band [44,45]. For $3d$ transition metals the $L_{2,3}$ edges are therefore dominated by $2p \rightarrow 3d$ transitions.

In the single particle description, the $L_{2,3}$ ELNES should be closely related to the LDOS of the unoccupied $3d$ states. However, comparison of the calculated d-projected-LDOS and $L_{2,3}$ EELS spectra of transition metal oxides show poor agreement [45]. This discrepancy is due to the strong overlap of the wavefunctions of the $2p$ hole and the $3d$ electrons, which results in large multiplet effects due to Coulomb and exchange interactions [46].

Since the $3d$ electrons are relatively tightly bound and the d bands are quite narrow, the $L_{2,3}$ edges in transition metal oxides can successfully be simulated using an approach based on atomic physics multiplet theory where solid-state effects are introduced as a perturbation [47]. This approach is valid for systems where the intra-atomic interactions are larger than the hybridization effects. An extensive review of multiplet effects is given by de Groot [46].

For $L_{2,3}$ edges, all interactions are dominated by the spin–orbit interaction in the $2p$ shell, which gives rise to the well separated L_3 ($2p_{3/2} \rightarrow 3d$) and L_2 ($2p_{1/2} \rightarrow 3d$) edges. Since the final $3d$ states are very narrow bands, sharp lines are visible at the edge threshold which are also referred to as "white lines" after being first discovered in X-ray absorption spectroscopy recorded on photographic film [48]. Corresponding to the $(2j+1)$ degeneracy of the initial core state, where j is the total angular momentum, the statistical white line branching ratio (L_3-to-L_2 intensity ratio) is 2:1. However, large variations from the statistical value are observed across the $3d$ transition row [45,49,50]. In $SrTiO_3$, for example, the Ti-$L_{2,3}$ edge (Figure 1) shows an apparent reversal of the branching ratio, with a more intense L_2 edge. This redistribution of intensity is due to multiplet effects and $3d$ spin–orbit coupling (for systems with partially filled $3d$ bands) [51]. In real experiments, the L_2/L_3 branching ratio is not a reliable measure of formal valence, both from the multiple competing effects that determine the ratio, and from the plural plasmon scattering that raises the L_2 edge as a function of sample thickness.

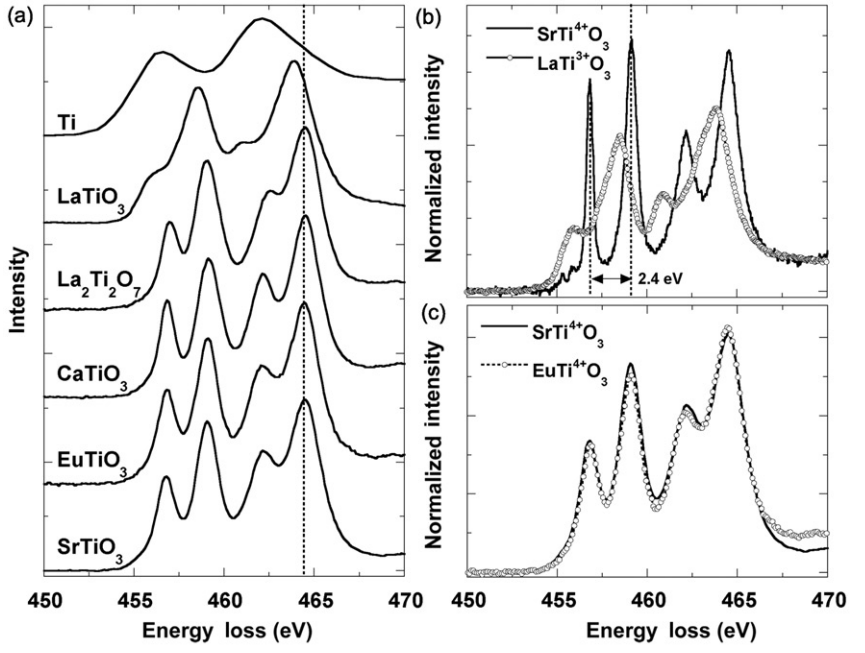

Figure 1. (a) Ti-$L_{2,3}$ edge EELS of various oxides and Ti metal. (b) Fingerprints of Ti^{4+} and Ti^{3+} demonstrating the sensitivity of the Ti-$L_{2,3}$ near edge fine structure to changes in the Ti valence. (c) Changes in the A-site cation (next nearest neighbor) has little effect on the Ti-$L_{2,3}$ fine structure for tetravalent Ti. (a, c) The individual Ti-L edges were recorded on the VG HB-501 100 kV dedicated STEM, which is equipped with a parallel electron energy loss spectrometer (Ti, $LaTiO_3$, $La_2Ti_2O_7$, $SrTiO_3$) or on the 200 kV FEI Tecnai F20-ST fitted with a monochromator and a Gatan imaging filter 865-ER ($CaTiO_3$, $EuTiO_3$). The energy resolution, as measured from the FWHM of the zero loss peak, was ~0.75 eV for Ti metal and ~0.6 eV for all other spectra in (a, c). The spectra in (b) were recorded on an FEI Tecnai F20 with the monochromator in filtered mode which improved the energy resolution to ~0.15 eV for $SrTiO_3$ and ~0.28 eV for $LaTiO_3$.

In multiplet calculations of the ELNES, solid-state effects are introduced as a perturbation. The most prominent effect of the solid is the crystal field, which breaks the symmetry around the excited atom. The atomic spectrum (spherical symmetry), which is obtained from atomic multiplet calculations, therefore needs to be projected onto the appropriate symmetry group. For simple perovskite oxides the transition metal is octahedrally coordinated by six oxygen atoms, i.e. O_h symmetry, which splits the degenerate $3d$ final states into two levels of t_{2g} (d_{xy}, d_{xz}, d_{yz}) and e_g ($d_{z^2}, d_{x^2-y^2}$) orbitals. In O_h symmetry, the e_g orbitals point to the ligands while the t_{2g} point in between, which results in stronger bonding of the e_g orbitals to the ligands and therefore a higher energy of the (antibonding) e_g states. Each of the two $L_{2,3}$ edges are therefore split into the lower-lying t_{2g} and higher-lying e_g levels. De Groot et al. [52] have pointed out that the splitting within the L_3 (and the L_2 edges) is related to, but not equal to, the crystal field splitting. Even for small crystal fields, an energy

splitting immediately appears, because other final states which were not accessible in spherical symmetry are now mixed in.

Direct comparison of atomic multiplet calculations (projected in the appropriate crystal field) and the experimentally measured $L_{2,3}$ edges would only work if the material is completely ionic. Transition metal oxides, however, have partially covalent character, which results in modification of the near-edge fine structure. This effect of the non-negligible hybridization of the transition metal with the ligand atoms, oxygen in our case, can be taken into account in the multiplet calculations by reducing the effective Coulomb and exchange parameters (Slater integrals) from their atomic values [46,53]. The intra-atomic interactions are thereby reduced due to solid-state effects.

The Ti-$L_{2,3}$ edges for various oxides and for Ti metal are shown in Figure 1a. For $SrTiO_3$ where the Ti atom is octahedrally coordinated, the combination of spin–orbit splitting and crystal field splitting gives rise to the expected four strong peaks and multiplet calculations of Ti^{4+}, i.e. $3d^0$, in perfect O_h symmetry shows good agreement with the experimental results [52]. A more complex multiplet structure is expected if the site-symmetry of the transition metal is reduced, e.g. from octahedral to tetragonal or if the occupancy of the 3*d* band in the ground state is increased from d^0 resulting in a larger number of final states as in $LaTiO_3$ where the formal valence of Ti is 3+ ($3d^1$ ground state configuration) [44,54]. The transition metal $L_{2,3}$ ELNES is therefore sensitive to the valency of the transition metal ion and its coordination.

A useful concept in ELNES is that of coordination "fingerprints" where the general form of the ELNES is predominantly sensitive to the nearest neighbor coordination [44]. This is most likely to occur on cations with strong contractions of the valence electrons. It implies that a detailed understanding of the DOS of complex materials is not necessary in order to interpret the ELNES for a specific edge. The detailed shape of the multiplet can instead be used to determine the valence of a transition metal ion, which is demonstrated in Figure 1a where only small variations in the Ti-$L_{2,3}$ edge fine-structure are visible for the tetravalent Ti in $SrTiO_3$, $EuTiO_3$, $CaTiO_3$ and $La_2Ti_2O_7$. The small changes in the Ti-$L_{2,3}$ edge fine-structure of these oxides could be due to changes in the local Ti site symmetry or due to variations in the covalency of the compounds [46,52,55]. In Figure 1b, fingerprints for Ti^{4+} and Ti^{3+} are shown. As the Ti valence decreases (or the number of 3*d* electrons increases) the Ti-$L_{2,3}$ edges shift to lower energies which is caused by changes in the electrostatic energy at the Ti site and the fine-structure changes due to the presence of a larger number of final states. Shifts of the $L_{2,3}$ edges to higher energies and changes in the fine-structure with increasing valency of the transition metal ion have previously been shown for various perovskite oxides [6,55–57].

2.2. *Trends in the O-K edges*

The O-*K* ELNES is sensitive to the local electronic structure and in particular to the chemical bond formed between the oxygens and their neighbors. Starting again with the dipole selection rule, transitions from the 1*s* core state to unoccupied states of *p*-symmetry are allowed and are closely related to the ELNES of the O-*K* edge.

For CuO it has been shown that up to ~15 eV above edge onset, the O-*K* edge is dominated by transitions to states of O 2*p* (not 3*p*) character [58]. The O-*K* edge is therefore typically described by O $1s \rightarrow 2p$ transitions. In a pure ionic picture, however, O^{2-} has a $1s^2 2s^2 2p^6$ configuration and the $1s \rightarrow 2p$ channel should be closed. But transition metal oxides are not fully ionic, and show a considerable covalent contribution. This covalency reduces the number of filled states with O 2*p* character and the channel for $1s \rightarrow 2p$ transitions opens up. The strength of the O-*K* edge signal close to the edge threshold therefore reflects the degree of covalency in the compound.

As discussed before, a core-hole is created during the excitation process which can have significant effects on the ELNES. At the O-*K* edge, however, the O 1*s* core-hole is generally well screened by the O 2*p* valence electrons [59], and has only small effects on the spectral shape. The O-*K* ELNES can therefore be interpreted on the basis of partial DOS calculations. This is in contrast to the previously discussed transition metal $L_{2,3}$ edges, which are dominated by multiplet effects due to the strong correlations between the 2*p* core-hole and the 3*d* electrons.

For 3*d* transition metal oxides it is generally accepted that the O-*K* threshold structure arises from covalent mixing of transition metal 3*d* and O 2*p* states, which introduces O *p*-character in unoccupied states of predominantly transition metal character [57,60–62]. Depending on the filling of the 3*d* bands and the local symmetry, the threshold structure may consist of one or several peaks which can be interpreted in terms of crystal field and exchange splitting [57,61].

Figure 3 shows a series of O-*K* edges for various oxides, which will be used to demonstrate some of the trends in the O-*K* ELNES of perovskite oxides. Starting with the well studied $SrTiO_3$ (separately shown in Figure 2), the bottom of the conduction band (and the first 5 eV of the O-*K* edge) is dominated by the empty Ti 3*d* states that are split into the t_{2g} and e_g subbands in the octahedral crystal field. The weak π hybridization of the Ti-3*d* t_{2g} with the O 2*p* orbitals results in the formation of a narrow band and a sharp peak A1 at the edge onset. The band corresponding to the stronger σ hybridization of Ti-3*d* e_g with O 2*p* orbitals is broader and is visible in the O-*K* edge as a much smaller second peak A2 [63]. Due to the strong dependence on hybridization effects, the O-*K* ELNES is sensitive to changes in the local transition metal geometry. This has been shown in both anatase and rutile TiO_2, where the distortions of the octahedra allow cation–cation and anion–anion interactions, with the net result of similar band widths of the t_{2g} and e_g bands [63].

When comparing the O-*K* edge of $SrTiO_3$ with that of $LaTiO_3$ large changes in the ELNES are visible (Figure 3). As La is substituted for Sr the Ti valence changes from 4+ to 3+, doping one electron per site into the empty Ti 3*d* band, i.e. $3d^0$ to $3d^1$ configuration. This decreases the number of unoccupied 3*d* states which is reflected in the O-*K* edge as a reduction in the intensity of the first peak. As a second electron is added to the 3*d* band for $LaVO_3$ ($3d^2$), the first peak decreases further. Finally, in $La_2Ti_2O_7$ a strong first peak is observed again, in accordance with a Ti valence of 4+. These trends show that the first ~5 eV beyond edge onset reflect the filling of the transition metal 3*d* bands and therefore the transition metal valence.

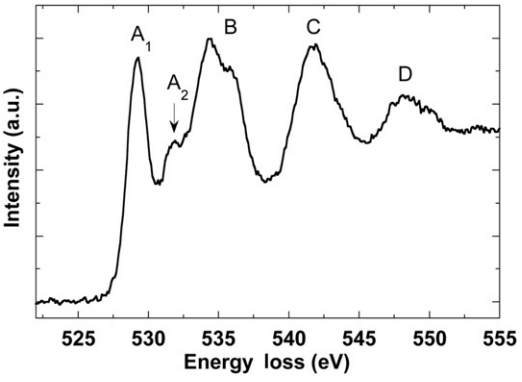

Figure 2. O-*K* edge EELS for $SrTiO_3$. The peaks in the spectrum are associated with O 2*p* orbitals hybridized with Ti 3*d* (A_1 and A_2), Sr 4*d* (B) and higher-energy metal states such as Sr 5*p* and Ti 4*sp* (C, D). The spectrum was recorded on the FEI Tecnai F20-ST STEM at an energy resolution of ~0.6 eV.

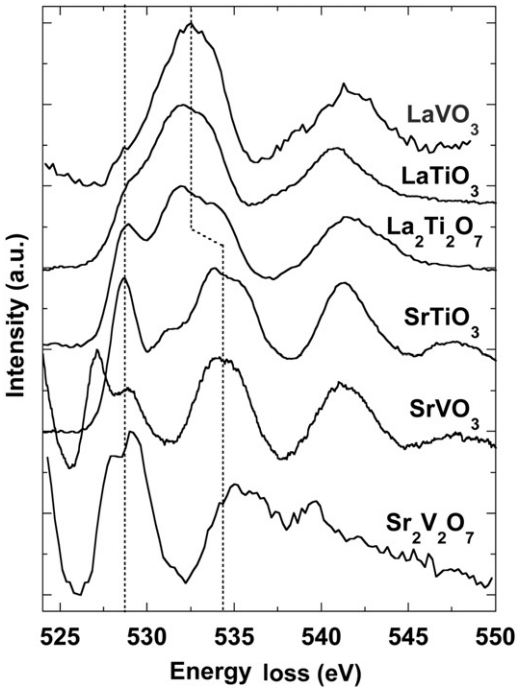

Figure 3. Trends in the O-*K* edge for a series of oxides. The features in the first ~5 eV beyond edge onset reflect the filling of the transition metal 3*d* bands and therefore the transition metal valence. The second main peak is dominated by the A-site cation and shifts to lower energies as Sr is substituted by La (right dotted line). The O-*K* edges for $LaVO_3$, $LaTiO_3$, $La_2Ti_2O_7$ and $SrTiO_3$ were recorded on the VG HB-501 STEM and the O-*K* edges for $SrVO_3$ and $Sr_2V_2O_7$ on the FEI Tecnai F20-ST STEM. The energy resolution, as measured from the FWHM of the zero loss peak, was ~0.8 eV for $LaVO_3$ and ~0.6 eV for all other spectra.

When comparing the O-*K* edges of $SrTiO_3$ and $LaTiO_3$, changes are not only found in the fine-structure at edge onset. Additionally, there is a large shift in the position of the second main peak. For $SrTiO_3$ this peak (peak B in Figure 2) has been related to bands of Sr 4*d* states hybridized with O 2*p*. The O-*K* ELNES therefore not only contains information about the valency of the transition metal ion, but also about the A-site cation. As Sr is replaced by La in $LaTiO_3$, the second peak shifts to lower energies now reflecting bands of mainly La 5*d* weight. This shift in the position of the second peak upon La for Sr substitution is shown in Figure 3 for a series of compounds and demonstrates that the second peak is dominated by the A-site cation. Note, however, that the position of the second main peak cannot be directly correlated with the position of the A-site cation *d* bands due to the potential overlap with the Ti 3*d*-e_g band [64], for which a larger dispersion is expected due to the stronger σ interactions with the ligands as mentioned above. Compared to $SrTiO_3$, this overlap is larger in the case of $LaTiO_3$, since the La 5*d* bands are shifted to lower energies. Finally, the third and fourth main peaks in $SrTiO_3$ (peaks C and D in Figure 2) are attributed to bands of higher-energy metal states such as Sr 5*p* and Ti 4*sp*, respectively [63].

In Figure 4, a collection of O-*K* edges for various oxides is given and will serve as a reference. Similar arguments as in the case of the titanates can also be made to explain the differences in the O-*K* ELNES of the two manganites $LaMnO_3$ and $SrMnO_3$ shown in Figure 4. Again, the second main peak (5–10 eV above edge onset), which is attributed to mainly Sr 4*d*/ La 5*d* bands, shifts to lower energies as Sr is replaced by La. The Mn valence change from 4+ to 3+ results in the reduction of the spectral weight at edge onset, in accordance with this region of the O-*K* edge being dominated by the Mn-3*d* bands. The observed O-*K* pre-peak structure is in agreement with previous results by Kurata et al. [57], who have extensively studied manganese oxides and interpreted the pre-peak structure with support of a molecular-orbital picture. For Mn^{4+}, a d^3 system, exchange splitting in addition to the crystal field splitting has to be taken into account [61]. The intense first O-*K* peak in $SrMnO_3$ can then be attributed to transitions to majority-spin e_g and minority-spin t_{2g} bands, which have similar energy positions due to the nearly identical values of exchange and crystal field splitting [57,61]. The second weaker peak is due to transitions to minority e_g states.

Compared to the O-*K* edge of $SrTiO_3$ the edge onset of $SrMnO_3$ shifts to lower energies, which is consistent with the fact that the Mn-3*d* states are located below the Ti-3*d* bands in $SrTiO_3$. Similarly, it has previously been shown that an additional shoulder at the O-*K* edge onset of $Ba_3Ti_2MnO_9$ compared to $BaTiO_3$ can be attributed to transitions to Mn 3*d* states [53].

For $NdNiO_3$ compared to $LaNiO_3$, and for $DyScO_3$ compared to $GdScO_3$ only small changes in the O-*K* ELNES are observed (Figure 4), because the 3*d* configuration does not change (d^7 for both nickelates and d^0 for both scandates). The small change in the position of the second peak is due to the substitution of the A-site cation.

Finally, it should be pointed out that the presence of oxygen vacancies in the material will damp out the O-*K* ELNES [22,65], which has to be taken into account when interpreting changes in the O-*K* fine-structure at perovskite oxide interfaces or around defects.

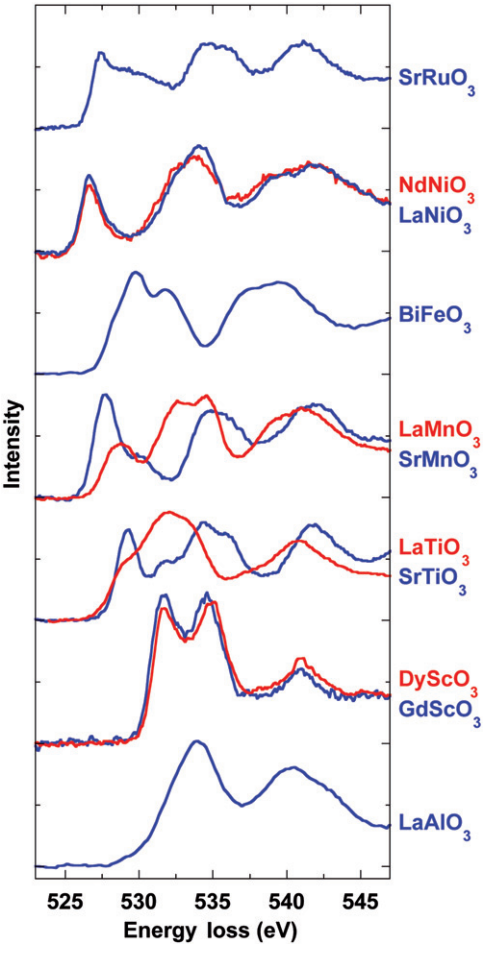

Figure 4. O-*K* edge EELS of various perovskite oxides. The O-*K* edge for $LaVO_3$ was recorded on the VG HB-501 STEM, all other spectra on the FEI Tecnai F20-ST STEM. The energy resolution, as measured from the FWHM of the zero loss peak, was ~0.6 eV.

3. Resolution limits in spectroscopic imaging

In HAADF imaging of thin samples, the spatial resolution is mainly determined by the size of the electron beam. As electron–optical aberrations are corrected, the probe-forming aperture can be opened up and the beam size can be reduced resulting in sub-angstrom beams. In spectroscopic imaging, however, the signal is based on inelastically scattered electrons and in addition to the probe size, the delocalization of inelastic scattering has to be taken into account. For incoherent inelastic scattering, i.e. when the collection semi-angle is large compared to the probe forming semi-angle [33,66], the signal becomes increasingly localized as the energy loss increases [67]. For spectroscopic imaging in an uncorrected system, this effect has been demonstrated in La maps of a layered manganite [24] and Si maps of Si_3N_4 [32].

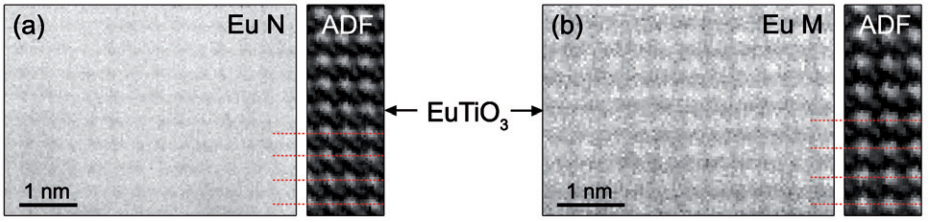

Figure 5. Delocalization effects in atomic resolution spectroscopic imaging. (a) Eu-$N_{4,5}$ (~135 eV) and (b) Eu-$M_{4,5}$ (~1100 eV) elemental maps of $EuTiO_3$ obtained from two individual spectroscopic images. A part of the simultaneously recorded HAADF image is shown for comparison on the right side of each map. The dotted lines (red online) indicate the position of Eu columns.

Note that for certain specimen thicknesses elastic scattering can strongly modify the inelastic signal [36,68].

Here, we show an example of delocalization effects in spectroscopic images recorded on a fifth order aberration corrected 100 keV NION UltraSTEM, which is equipped with a Gatan Enfina electron energy-loss spectrometer. The convergence semi-angle was 34 mrad and the collection semi-angle 77 mrad. The sample study was a thin film of $EuTiO_3$ grown on $DyScO_3$ by molecular beam epitaxy [72]. Europium elemental maps of $EuTiO_3$ (Figure 5) were extracted from two individual spectroscopic images by integrating over the background subtracted Eu-$N_{4,5}$ edges at ~135 eV and the Eu-$M_{4,5}$ edges at ~1100 eV, respectively. We find a clear improvement of the lattice fringe contrast for larger energy losses, i.e. the Eu-$M_{4,5}$ map (Figure 5b). The contrast of the 3.9 Å lattice fringes, which are associated with the {001} planes in $EuTiO_3$, decreases by a factor of 4 from ~16% in the Eu-$M_{4,5}$ map to ~4% in the Eu-$N_{4,5}$ map. The contrast was calculated by averaging the entire image into a single line profile. The fringe contrast is reduced from that expected from a single line profile due to random scan noise and image drift.

In order to characterize these delocalization effects in more detail, we have performed quantum mechanical calculations of inelastic scattering within the dipole approximation based on previous work by Kohl and Rose [34] and Muller and Silcox [33]. For comparison with experiment, the parameters were set to match the conditions of our 100 keV NION UltraSTEM but ignoring lens aberrations. The introduction of aberrations will not change the qualitative picture. Two measures of resolution, the full width at half maximum (FWHM) and the diameter of the disk containing 80% of the scattered electrons are shown in Figure 6a as a function of energy loss. The FWHM is nearly constant across the calculated energy loss range (Figure 6b) and is close to the size of the incident electron probe. The disk containing 80% of the scattered electrons, however, increases dramatically as the energy loss decreases. Using the 80% radius, rather than the limit of the information transfer or the FWHM, as a measure of resolution automatically takes into account the practical limit set by the signal to noise ratio. It is therefore a more relevant measure of resolution than the FWHM or the information limit for analytical measurements or when interdiffusion is of interest. As demonstrated by the dramatic increase in the 80% radius for low energy losses, inelastic delocalization adds large

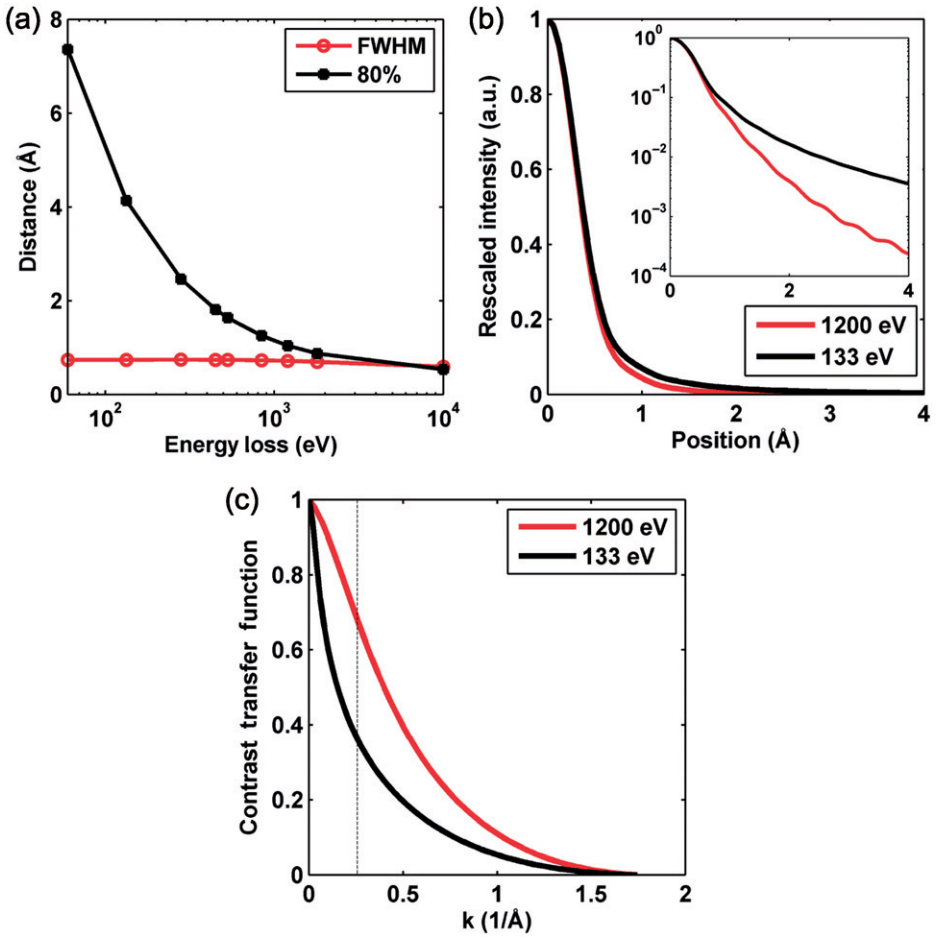

Figure 6. Delocalization in inelastic scattering for an aberration free 100 kV STEM at zero defocus, with a 34 mrad convergence semi-angle and a 77 mrad collection semi-angle calculated within the dipole approximation according to [34,33]. (a) Measures of spatial resolution as a function of energy loss: the full width at half maximum (FWHM) of the inelastic scattering profile and the radius of the disk containing 80% of the scattered electrons. (b) The rescaled scattering cross-section as a function of the position of the incident beam for an energy loss of 133 eV and 1200 eV, respectively. In the inset, the intensity is replotted on a log scale. (c) The contrast transfer functions of the inelastic scattering profiles in (b). The dashed line labels the 3.9 Å lattice spacing which is associated with the {001} planes in $EuTiO_3$.

tails to the point spread function [33]. This gives rise to a reduction of the fringe contrast in atomic resolution spectroscopic images as shown by the damping of the contrast transfer function for an energy loss of 133 eV compared to 1200 eV (Figure 6). Depending on the signal-to-noise ratio in these images, the reduction in contrast can limit the achievable spatial resolution. When estimating the resolution in spectroscopic imaging of a thin specimen one therefore has to take into account

the incident probe size as well as the reduction of the fringe contrast at low energy losses due to inelastic delocalization and the signal to noise ratio of the image.

4. Spectroscopic imaging of atomic-scale interdiffusion in $LaVO_3/SrTiO_3$ multilayers

In electron microscopy, it is often difficult to distinguish between true intermixing and the apparent broadening of an interface due to the shape of the electron probe or its tails. In addition, the contrast in HAADF images is dominated by the heavier atoms which can mask effects due to the intermixing of lighter atoms. However, the additional chemical information obtained from atomic-resolution spectroscopic imaging can be used to directly detect chemical intermixing and its impact on the electronic structure of an interface.

Here, we present results on the microscopic structure of a $LaVO_3/SrTiO_3$ multilayer using spectroscopic imaging. The heterostructure was grown by pulsed laser deposition (PLD), one of the growth techniques which allows high quality materials with complex structures to be fabricated. Atomic-layer precision in PLD of complex oxides has been demonstrated [4]. For most systems, however, there are intrinsic limitations to the abruptness of an interface, such as polar discontinuities which can drive electronic as well as atomic reconstructions at the interface [4,69,70]. In $LaVO_3/SrTiO_3$ multilayers, Sr surface segregation during the growth can greatly affect the interface abruptness and lead to a growth asymmetry, with diffuse lower and atomically abrupt upper vanadate interfaces [71]. Spectroscopic imaging of a similar $LaVO_3/SrTiO_3$ multilayer now reveals that the upper interface is atomically abrupt for the A-site (Sr/La) cations only, while there is a small degree of intermixing for the B-site cations (Ti/V).

Spectroscopic imaging was performed on the NION UltraSTEM, with a 34 mrad convergence semi-angle and a collection semi-angle of 77 mrad. The spectra were recorded at a dispersion of 0.3 eV/channel which gives a spectral range of ~400 eV and allows the Ti-$L_{2,3}$, V-$L_{2,3}$, O-K and La-M_5 edges to be recorded simultaneously. The dwell time was 10 msec/spectrum, sufficient to resolve the expected four peaks in the Ti-L edge of $SrTiO_3$ (Figure 7d). The full spectroscopic image contains 128x375 spectra and was recorded in 25 minutes without drift correction.

Individual elemental maps were obtained by subtracting the background of the respective edges and integrating over the first ~10 eV of the near-edge fine structure at each point in the spectroscopic image. The La elemental map and red-blue false color B-site map, obtained by combining the Ti (red channel) and V (blue channel) maps, of the $LaVO_3/SrTiO_3$ multilayer are shown in Figures 7b and c, respectively. Both the elemental maps and the simultaneously acquired HAADF image, shown in Figure 7a, demonstrate the remarkable stability of the microscope, keeping in mind that no sample drift correction has been performed during the measurement.

In the HAADF image, the upper vanadate interfaces appear atomically abrupt while the lower interfaces are more gradual, which is consistent with our previous results on similar multilayers [71]. What can be learned from the elemental maps? The growth asymmetry observed in the HAADF image is also clearly visible in the La map, which is not surprising because the HAADF image is dominated by the

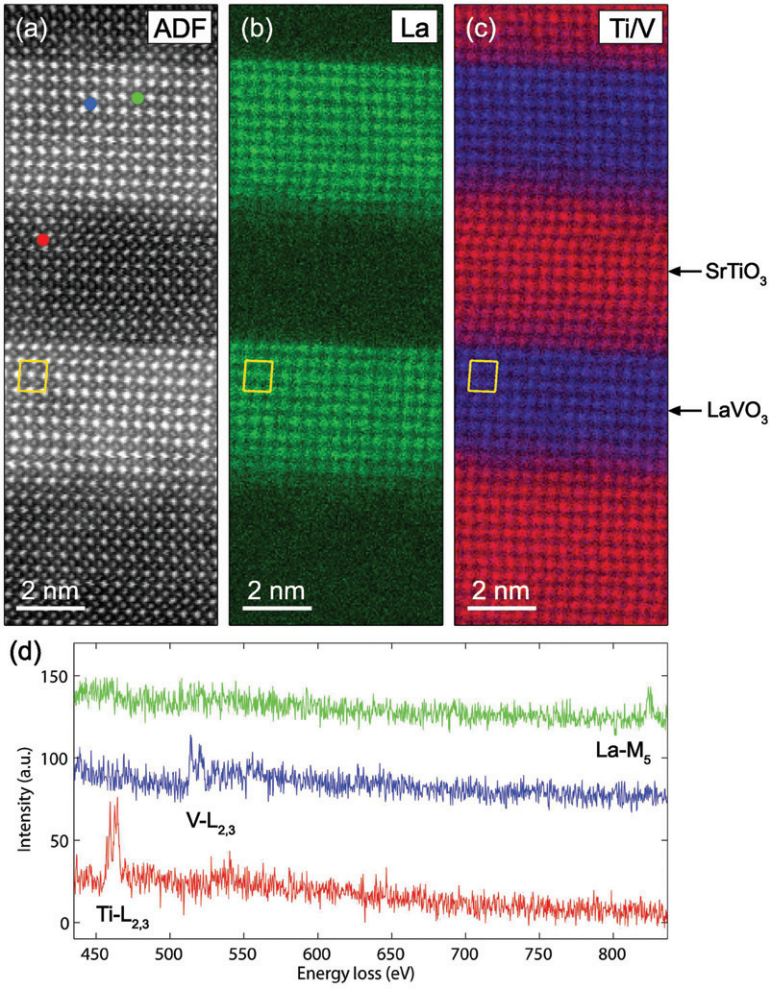

Figure 7. Atomic resolution spectroscopic imaging of $LaVO_3/SrTiO_3$ multilayers. (a) Simultaneously recorded HAADF image, (b) La elemental map and (c) red-blue false color B-site map, obtained by combining the Ti (red channel) and V (blue channel) maps, of the multilayer. While the La elemental map shows an atomically abrupt upper vanadate interface the purple band in the B-site map indicated Ti/V intermixing. The yellow boxes are markers to track the position of the La columns in the individual elemental maps and show that the V lattice is properly offset. (d) Individual EELS spectra extracted from the spectroscopic map and offset vertically for clarity. The color-coded dots in (a) indicate the locations where the EELS spectra were recorded.

distribution of the La atoms, the heaviest in the structure. The abruptness of the upper interfaces also gives an upper limit to the influence of the probe, i.e. beam spreading or probe tails on the resolution in these chemical maps. Keeping that in mind, it is surprising to not find the same abruptness in the vanadium distribution at the upper interfaces. The false-color B-site map shows purple layers not only at the

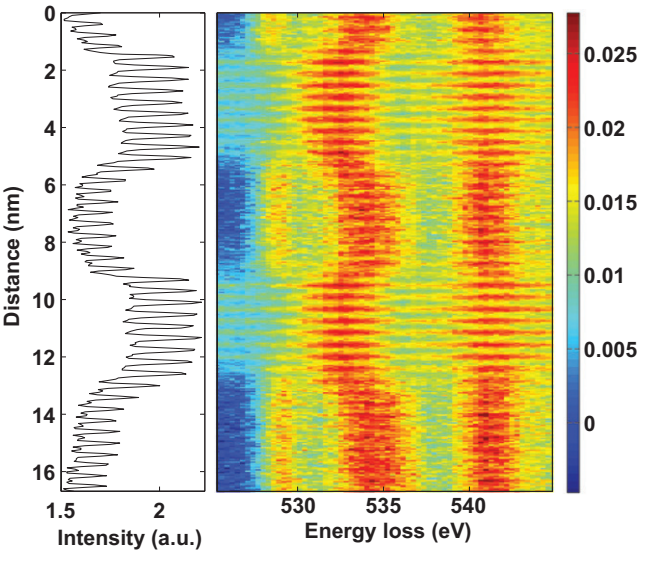

Figure 8. Evolution of the O-*K* edge fine structure across the $LaVO_3/SrTiO_3$ multilayer. (Left) Horizontally-integrated line profile of the HAADF signal that was simultaneously recorded with the EELS map. (Right) The corresponding O-*K* edges. The spectra are gain corrected and averaged parallel to the interfaces to improve the signal-to-noise ratio. The background has been removed by fitting a powerlaw to the O-*K* pre-edge in $SrTiO_3$. In $LaVO_3$, this is hampered by the presence of the V-*L* edges in the O-*K* pre-edge region, so the same powerlaw dependence as in $SrTiO_3$ has been used, but scaled according to the V-*L* pre-edge intensity.

lower but also at the upper vanadate interfaces indicating vanadium/titanium intermixing at both interfaces. The amount of intermixing at the upper interface was quantified by averaging the vanadium concentration parallel to the interfaces and then fitting the concentration profile with a series of Gaussians each separated by a unit cell. We find that the vanadium that has intermixed amounts to a full atomic layer in $LaVO_3$ and is distributed over four unit cells in the nominal $SrTiO_3$ layer above. Where is the vanadium coming from? With the advantage of atomic resolution elemental maps, the stacking sequence at an interface can directly be read off. Here, the top La layer can be used as a marker. By comparing the La and the B-site maps, we find the upper interface to be a mixture of $VO_2/LaO/VO_2$ and $VO_2/LaO/TiO_2$. From growth the $LaVO_3$ was expected to be VO_2 terminated, however, due to intermixing during the growth the vanadium in the last layer has diffused into the $SrTiO_3$ layer above. Surprisingly, it is only the vanadium in the top VO_2 layer that has intermixed. There is no detectable intermixing for the VO_2 layer one unit cell below. Because of the selective intermixing of only the top VO_2 layer which is now spread out over four unit cells in the $SrTiO_3$, the interface appears mostly $VO_2/LaO/TiO_2$ terminated which would result in an n-type interface. The vanadium that has diffused into the $SrTiO_3$, however, cannot be ignored and care has to be taken when determining the interface type from spectroscopic images.

For completeness, let us look at the lower vanadate interfaces. Both the La as well as the V concentration profiles are more gradual compared to the upper

interfaces and a clear offset between the La and V profiles is found. This offset is a factor of 3 larger than the expected 0.5 unit cell, which has been observed previously using spatially resolved EELS along a line across the interface, and is indicative of Sr surface segregation as discussed in Ref. [71].

Finally, variations in the EELS edge fine-structure can be observed. Figure 8 shows the HAADF intensity profile and the evolution of the O-*K* edge fine structure across the multilayer. To increase the signal-to-noise, all spectra parallel to the interfaces have been averaged. Note that the O-*K* pre-edge in the vanadate layer is nonzero due to the proximity of the V-$L_{2,3}$ edges [6] with its two main peaks at ~514.5 eV and ~521 eV.

The variations in the O-*K* ELNES are dominated by two effects: (1) the damping of the first peak at ~529.2 eV and (2) the shift of the second main peak to lower energies when crossing the interface from $SrTiO_3$ to $LaVO_3$. These changes are in agreement with the trends of the O-*K* fine structure discussed in a previous section. As the filling of the 3*d* band is increased from no electrons in $SrTiO_3$ to two electrons in $LaVO_3$, the first peak decreases. The shift of the second peak is, on the other hand, related to the substitution of Sr with La atoms on the A-site.

5. Conclusions

With recent advances in electron microscopy, in particular the successful implementation of fifth-order aberration correction, atomic-resolution 2D imaging of composition and bonding of buried interfaces and nanostructures is now possible. However, a good understanding of the near-edge fine structure of core-loss spectra is essential. For perovskite oxides it is the fine structure of the O-*K* and the transition-metal $L_{2,3}$ edges that are important and they are therefore reviewed here. Transition metal $L_{2,3}$ edges are dominated by atomic multiplet effects due to the strong coupling between the 2*p* core-hole and the 3*d* electrons with, however, strong sensitivity to the symmetry of the surrounding crystal field. The transition metal $L_{2,3}$ edge fine structure is therefore a powerful probe of the valency and the coordination of the transition metal atom. For the O-*K* edge, on the other hand, the 1*s* core-hole has only small effects on the spectral shape and it can therefore be interpreted on the basis of partial DOS calculations. The O-*K* edge fine structure for transition metal oxides can be divided into three regions. The features within the first ~5 eV above edge onset are dominated by transition metal 3*d* states and are therefore sensitive to the valency of the transition metal ion. The peaks 5–10 eV above edge onset are attributed to states derived from oxygen *p* and the A-site cation *d* orbitals. At higher energies the fine structure is dominated by bands of higher-energy metal states. A large collection of O-*K* edge "fingerprints" for perovskite oxides was established and can be used as reference for future work.

Demonstrating the capability of the technique, we have performed spectroscopic imaging on a $LaVO_3/SrTiO_3$ multilayer. While the HAADF image suggests atomically abrupt upper vanadate interfaces, spectroscopic imaging reveals atomic-scale interdiffusion of the B-site cations (V/Ti).

When estimating the resolution in spectroscopic imaging of a thin specimen, one has to take into account the incident probe size, inelastic delocalization effects and

the signal-to-noise ratio of the image. While atomic-resolution spectroscopic imaging is possible for high energy losses, delocalization in inelastic scattering adds long tails to the point spread function as the energy loss decreases. These tails cause a damping of the contrast transfer function. Atomic-resolution is lost when the fringe contrast is damped below the signal-to-noise ratio.

Acknowledgements

We thank M. Nakayama, S. Tsuda, T. Zhao, R. Ramesh and J.D. Brock for providing samples used in the EELS fine-structure study. M. Thomas and E.J. Kirkland are acknowledged for technical support with the NION UltraSTEM. We thank R. Erni for his help with the monochromated FEI Tecnai F20 at NCEM where the monochromated Ti-*L* edge spectrum of lanthanum titanate was recorded. The work at Cornell (LFK, HLX, DGS, DAM) was supported by the Cornell Center for Materials Research (NSF No. DMR-0520404 and No. IMR-0417392) with additional support from the Semiconductor Research Corporation, the Army Research Office (ARO W911NF0910415) and the ONR EMMA MURI. JHL acknowledges support by the National Science Foundation through the MRSEC program (NSF No. DMR-0820404).

References

[1] C.H. Ahn, J.M. Triscone and J. Mannhart, Nature 424 (2003) p.1015.
[2] E. Dagotto, Science 309 (2005) p.257.
[3] H.Y. Hwang, MRS Bull. 31 (2006) p.28.
[4] A. Ohtomo, D.A. Muller, J.L. Grazul and H.Y. Hwang, Nature 419 (2002) p.378.
[5] A. Ohtomo and H.Y. Hwang, Nature 427 (2004) p.423.
[6] L.F. Kourkoutis, Y. Hotta, T. Susaki, H.Y. Hwang and D.A. Muller, Phys. Rev. Lett. 97 (2006) p.256803.
[7] A. Brinkman, M. Huijben, M. Van Zalk, J. Huijben, U. Zeitler, J.C. Maan, W.G. Van Der Wiel, G. Rijnders, D.H.A. Blank and H. Hilgenkamp, Nat. Mater. 6 (2007) p.493.
[8] N. Reyren, S. Thiel, A.D. Caviglia, L.F. Kourkoutis, G. Hammert, C. Richter, C.W. Schneider, T. Kopp, A.-S. Ruetschi, D. Jaccard, M. Gabay, D.A. Muller, J.-M. Triscone and J. Mannhart, Science 317 (2007) p.1196.
[9] A. Gozar, G. Logvenov, L.F. Kourkoutis, A.T. Bollinger, L.A. Giannuzzi, D.A. Muller and I. Bozovic, Nature 455 (2008) p.782.
[10] K.S. Takahashi, M. Kawasaki and Y. Tokura, Appl. Phys. Lett. 79 (2001) p.1324.
[11] A.V. Crewe, J. Wall and J. Langmore, Science 168 (1970) p.1338.
[12] J. Wall, J. Langmore, M. Isaacson and A.V. Crewe, Proc. Natl. Acad. Sci. USA 71 (1974) p.1.
[13] A. Howie, J. Microsc. 117 (1979) p.11.
[14] M.M.J. Treacy and S.B. Rice, J. Microsc. 156 (1989) p.211.
[15] E.J. Kirkland, R.F. Loane and J. Silcox, Ultramicroscopy 23 (1987) p.77.
[16] R.F. Loane, E.J. Kirkland and J. Silcox, Acta Crystallogr. Sect. A 44 (1988) p.912.
[17] J. Fertig and H. Rose, Optik 59 (1981) p.407.
[18] P.M. Voyles, J.L. Grazul and D.A. Muller, Ultramicroscopy 96 (2003) p.251.
[19] S.E. Hillyard and J. Silcox, Ultramicroscopy 58 (1995) p.6.
[20] D.D. Perovic, C.J. Rossow and A. Howie, Ultramicroscopy 52 (1993) p.353.
[21] Z. Yu, J. Appl. Phys. 95 (2004) p.3362.

[22] D.A. Muller, N. Nakagawa, A. Ohtomo, J.L. Grazul and H.Y. Hwang, Nature 430 (2004) p.657.
[23] A.V. Crewe, Science 154 (1966) p.729.
[24] K. Kimoto, T. Asaka, T. Nagai, M. Saito, Y. Matsui and K. Ishizuka, Nature 450 (2007) p.702.
[25] M. Isaacson and D. Johnson, Ultramicroscopy 1 (1975) p.33.
[26] C. Jeanguillaume and C. Colliex, Ultramicroscopy 28 (1989) p.252.
[27] P.E. Batson, Nature 366 (1993) p.727.
[28] D.A. Muller, Y. Tzou, R. Raj and J. Silcox, Nature 366 (1993) p.725.
[29] M. Haider, S. Uhlemann, E. Schwan, H. Rose, B. Kabius and K. Urban, Nature 392 (1998) p.768.
[30] P.E. Batson, N. Dellby and O.L. Krivanek, Nature 418 (2002) p.617.
[31] D.A. Muller, L.F. Kourkoutis, M. Murfitt, J.H. Song, H.Y. Hwang, J. Silcox, N. Dellby and O.L. Krivanek, Science 319 (2008) p.1073.
[32] K. Kimoto, K. Ishizuka and Y. Matsui, Micron 39 (2008) p.257.
[33] D.A. Muller and J. Silcox, Ultramicroscopy 59 (1995) p.195.
[34] H. Kohl and H. Rose, Adv. Electron. Electron Phys. 65 (1985) p.173.
[35] A.J. D'Alfonso, S.D. Findlay, M.P. Oxley and L.J. Allen, Ultramicroscopy 108 (2008) p.677.
[36] M. Bosman, V.J. Keast, J.L. Garcia-Munoz, A.J. D'Alfonso, S.D. Findlay and L.J. Allen, Phys. Rev. Lett. 99 (2007) p.086102.
[37] A. Howie, Proc. R. Soc. A 271 (1963) p.268.
[38] P. Stallknecht and H. Kohl, Ultramicroscopy 66 (1996) p.261.
[39] D.A. Muller, Nat. Mater. 8 (2009) p.263.
[40] K. Suenaga, Y. Sato, Z. Liu, H. Kataura, T. Okazaki, K. Kimoto, H. Sawada, T. Sasaki, K. Omoto, T. Tomita, T. Kaneyama and Y. Kondo, Nat. Chem. 1 (2009) p.415.
[41] J.C.H. Spence, Rep. Prog. Phys. 69 (2006) p.725.
[42] P. Rez and D.A. Muller, Annu. Rev. Mater. Sci. 38 (2008) p.535.
[43] J.E. Muller and J.W. Wilkins, Phys. Rev. B 29 (1984) p.4331.
[44] V.J. Keast, A.J. Scott, R. Brydson, D.B. Williams and J. Bruley, J. Microsc. 203 (2001) p.135.
[45] J. Fink, T. Muller-Heinzerling, B. Scheerer, W. Speier, F.U. Hillebrecht, J.C. Fuggle, J. Zaanen and G.A. Sawatzky, Phys. Rev. B 32 (1985) p.4899.
[46] F.M.F. de Groot, Coord. Chem. Rev. 249 (2005) p.31.
[47] F.M.F. de Groot, J.C. Fuggle, B.T. Thole and G.A. Sawatzky, Phys. Rev. B 42 (1990) p.5459.
[48] P.S.P. Wei and F.W. Lytle, Phys. Rev. B 19 (1979) p.679.
[49] R.D. Leapman, L.A. Grunes and P.L. Fejes, Phys. Rev. B 26 (1982) p.614.
[50] W.G. Waddington, P. Rez, I.P. Grant and C.J. Humphreys, Phys. Rev. B 34 (1986) p.1467.
[51] F.M.F. de Groot, Physica B 208-209 (1995) p.15.
[52] F.M.F. de Groot, J.C. Fuggle, B.T. Thole and G.A. Sawatzky, Phys. Rev. B 41 (1990) p.928.
[53] G. Radtke, C. Maunders, S. Lazar, F.M.F. de Groot, J. Etheridge and G.A. Botton, J. Solid State Chem. 178 (2005) p.3426.
[54] J.P. Crocombette and F. Jollet, J. Phys. Condens. Matter 6 (1994) p.10811.
[55] A.S. Sefat, G. Amow, M.-Y. Wu, G.A. Botton and J.E. Greedan, J. Solid State Chem. 178 (2005) p.1008.
[56] M. Abbate, F.M.F. de Groot, J.C. Fuggle, A. Fujimori, Y. Tokura, Y. Fujishima, O. Strebel, M. Domke, G. Kaindl, J. van Elp, B.T. Thole, G.A. Sawatzky, M. Sacchi and N. Tsuda, Phys. Rev. B 44 (1991) p.5419.

[57] H. Kurata and C. Colliex, Phys. Rev. B 48 (1993) p.2102.
[58] M. Grioni, M.T. Czyzyk, F.M.F. de Groot, J.C. Fuggle and B.E. Watts, Phys. Rev. B 39 (1989) p.4886.
[59] I. Davoli, A. Marcelli, A. Bianconi, M. Tomellini and M. Fanfoni, Phys. Rev. B 33 (1986) p.2979.
[60] L.A. Grunes, R.D. Leapman, C.N. Wilker, R. Hoffmann and A.B. Kunz, Phys. Rev. B 25 (1982) p.7157.
[61] F.M.F. de Groot, M. Grioni, J.C. Fuggle, J. Ghijsen, G.A. Sawatzky and H. Petersen, Phys. Rev. B 40 (1989) p.5715.
[62] M. Abbate, F.M.F. de Groot, J.C. Fuggle, A. Fujimori, O. Strebel, F. Lopez, M. Domke, G. Kaindl, G.A. Sawatzky, M. Takano, Y. Takeda, H. Eisaki and S. Uchida, Phys. Rev. B 46 (1992) p.4511.
[63] F.M.F. de Groot, J. Faber, J.J.M. Michiels, M.T. Czyzyk, M. Abbate and J.C. Fuggle, Phys. Rev. B 48 (1993) p.2074.
[64] J. van Elp and A. Tanaka, Phys. Rev. B 60 (1999) p.5331.
[65] R.F. Klie and N.D. Browning, Appl. Phys. Lett. 77 (2000) p.3737.
[66] M.P. Oxley, E.C. Cosgriff and L.J. Allen, Phys. Rev. Lett. 94 (2005) p.203906.
[67] R.F. Egerton, *Electron Energy-Loss Spectroscopy in the Electron Microscope*, 2nd ed., Plenum Press, New York, 1996.
[68] P. Wang, A.J. D'Alfonso, S.D. Findlay, L.J. Allen and A.L. Bleloch, Phys. Rev. Lett. 101 (2008) p.236102.
[69] N. Nakagawa, H.Y. Hwang and D.A. Muller, Nat. Mater. 5 (2006) p.204.
[70] S. Okamoto and A.J. Millis, Nature 428 (2004) p.630.
[71] L.F. Kourkoutis, D.A. Muller, Y. Hotta and H.Y. Hwang, Appl. Phys. Lett. 91 (2007) p.163101.
[72] J.H. Lee, L. Fang, E. Vlahos, X. Ke, Y.W. Jung, L.F. Kourkoutis, J.-W. Kim, P.J. Ryan, T. Heeg, M. Roeckerath, V. Goian, M. Bernhagen, R. Uecker, P.C. Hammel, K.M. Rabe, S. Kamba, J. Schubert, J.W. Freeland, D.A. Muller, C.J. Fennie, P.E. Schiffer, V. Gopalan, E. Johnston-Halperin and D.G. Schlom, Nature 466 (2010) p.954.